This is the Pre-Published Version.

This document is the Accepted Manuscript version of a Published Work that appeared in final form in ACS Applied Nano Materials, copyright © 2025 American Chemical Society after peer review and technical editing by the publisher. To access the final edited and published work see https://doi.org/10.1021/acsanm.5c00964.

A Soft Robot Based on Charged Spiropyran Amphiphilic Supramolecular Nanoassembly for Macroscopic Actuation

Ka-Lung Hung,[a] Wai-Ki Wong,[a,b] Ming-Hin Chau,[a] Jerry Chun-Kit Yau,[a] Takashi Kajitani,[c] Shaoyu Chen,[d] and Franco King-Chi Leung*[a,b]*

[a]Mr. K.-L. Hung, Mr. J. C.-K. Yau, Mr. W.-K. Wong, Mr. M.-H. Chau, Prof. Dr. F. K.-C. Leung

State Key Laboratory of Chemical Biology and Drug Discovery, Research Institute for Future Food, Department of Applied Biology and Chemical Technology, The Hong Kong Polytechnic University, Hong Kong, China

E-mail: kingchifranco.leung@polyu.edu.hk

[b]Mr. W.-K. Wong, Prof. Dr. F. K.-C. Leung

Centre for Eye and Vision Research 17W Hong Kong Science Park, Hong Kong, China.

[c]Dr. T. Kajitani

Core Facility Center, Research Infrastructure Management Center,

Institute of Science Tokyo, 4259 Nagatsuta, Midori-ku, Yokohama 226-8501, Japan.

[d]Prof. Dr. S. Chen

School of Fashion and Textiles, The Hong Kong Polytechnic University, Hong Kong, China
E-mail: shaoyu.chen@polyu.edu.hk

Abstract

Biomimetic motion has advanced soft robotic materials. Common photoresponsive polymeric materials can sustain soft actuating robotic functions, while supramolecular soft robotics provide for unprecedented structural and functional roles, *e.g.*, stimuli-responsiveness, intrinsic supramolecular dynamicity, and bioactive cell-material interfaces. However, high structural requirements of hierarchical supramolecular assembly are crucial for fabrications of supramolecular soft robotics, limiting its technological developments. We demonstrate a generation of supramolecular soft robotic without high orientation order and structural uniformity, in sustaining macroscopic actuation. Highly charged supramolecular nanoassembly of spiropyran amphiphiles entraps water at macroscopic state and release water upon photoisomerization, and resultingly, enable macroscopic soft actuating robotic functions.

Keywords: Supramolecular Soft Robotic, Photoresponsive Amphiphile, Spiropyran, Hydrogel, Supramolecular Assembly

1. Introduction

Shape transformations and motions, induced by external stimulations, are sophisticated but commonly found in nature that is vital for living organisms with endowed movement and actuating functions.[1–3] Biological systems are empowered with precisely controlled movements, *e.g.*, calcium ion gradient controlled muscle contraction in animals,[4] while biomimetic motions and shape transformations of artificial soft actuating robotics are controlled with excellent tunabilities.

Polymeric liquid crystals,[5–9] elastomers,[6,10] and hydrogels,[11–18] are the key soft matters to sustain soft robotic functions. Different external stimulations, *e.g.*, heat, ion, humidity, magnetic field, and light, induce morphological transformations of polymeric hydrogels by changing their volume, structure, and shape.[19–24] Among all stimulations, light serves as a non-invasive method with high-temporal, high-spatial precisions, and tunabilities in wavelength and intensity for driving soft actuating robotics. Supramolecular soft robotics constructed by supramolecular interactions, has emerged as a promising alternative to soft actuating robotics with various polymeric backbones, in considerations of the stimuli-responsiveness, supramolecular dynamicity, and bioactive cell-material interfaces.[21,22,25–27] These unique and unprecedented functional properties of supramolecular soft robotics have shed light on the next generation of soft actuating robotics.

Hierarchical supramolecular assembly, served as the key fabrication strategy of supramolecular soft robotics, enable synchronization of molecular motions along higher hierarchical nanostructures, accumulation of strain, and amplification of motions to macroscopic level. Feringa reported the first supramolecular soft robotic through hierarchical supramolecular assembly of motor amphiphiles, in sustaining macroscopic actuating function upon UV-light irradiation.[28] High nanostructural orientation and uniformity of the hierarchical supramolecular assembly were identified as the key structural parameters, in enabling macroscopic actuations, reported by Leung and Feringa.[29,30] Recently, phenylazothiazole amphiphiles were demonstrated to assemble into nanofibers and to further align unidirectionally into a hierarchical supramolecular assembly, enabling efficient photoenergy conversion into morphological transformations with the fastest actuation speed, reported by our team.[31] Structural significances of the high orientational order in the hierarchical supramolecular assemblies of supramolecular soft robotic were further validated.

On the contrary, hierarchical supramolecular assembly of stiff-stilbene,[32,33] azobenzene,[34] donor-acceptor Stenhouse adducts,[35,36] and indigo,[37] featured with limited orientation order and structural uniformity, can only sustain isotropic shrinking and morphological transformations, upon photoirradiation. However, high structural requirements of supramolecular soft robotic is significantly hampering its rapid technological development. Alternatively, most of the molecular design of negatively charged spiropyran-photoacid were featured with a sulfonate group attached to the indolinium nitrogen, due to synthetic simplicity. To maximize microphase separation of molecular design of spiropyran amphiphile, hydrophilic group should be implemented at the position of hydroxyl-indolinium, to afford potential nanoassembly with large aspect-ratio. Intrinsic geometric structural transformations of spiropyran switch enable significant supramolecular transformation of formed nanoassembly at microscopic length-scale. Herein, we designed and synthesized a spiropyran amphiphile (**SPA**), featured with a sulphate group at the position of hydroxyl-indolinium. (Figure 1 and Scheme S1). By optimizing pH of **SPA**, the *open*-form of **SPA** (**SPA$_{Open}$**) can be the major component and form highly charged supramolecular nanoassembly, which can be controlled systematically by cyan- or green-light irradiation, which is the first supramolecular soft robotic driven by green-light. Macroscopic soft scaffold of **SPA$_{Open}$** (1.0 – 5.0 weight% (wt.%)) can be obtained to efficiently entrap water. The macroscopic soft scaffold of **SPA$_{Open}$** can be actuated toward to the light source, while the actuation mechanism is meticulously interpreted with X-ray diffraction (XRD), atomic force microscopy (AFM), optical, and electron microscopies. Entrapped water in macroscopic soft scaffold of **SPA$_{Open}$** is released upon photoisomerization from highly charged **SPA$_{Open}$** to **SPA$_{Closed}$**. Though the high dynamicity of macroscopic soft scaffold of **SPA$_{Open}$** cannot enable cell attachment on the highly charged surface of the scaffold, limited cytotoxicity of **SPA** nanostructures has been confirmed. By elucidation the

key design of supramolecular-based spiropyran hydrogels, ultimately, this could open up new prospects toward technological advancements in photoresponsive hydrogels and future soft robotic systems.

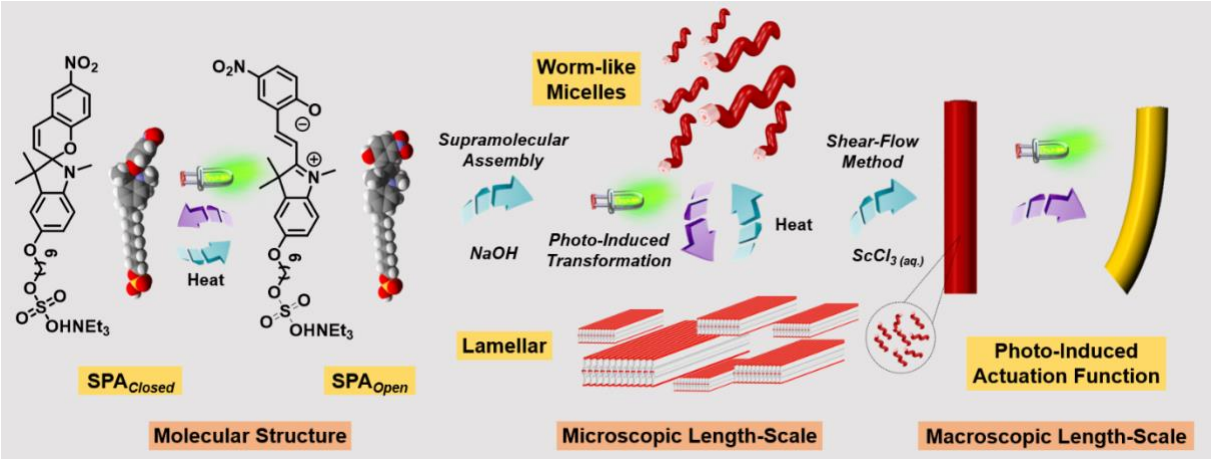

Figure 1. Molecular structure of spiropyran amphiphile and the macroscopic actuation process driven by cyan- and green-light through supramolecular nanoassembled structures in the macroscopic soft scaffold.

2. Results and Discussion

2.1. Photoisomerization and Thermal Back Processes of SPA in Organic and Aqueous Media

Photoisomerization processes of **SPA** were examined by UV-vis spectroscopy. A methanol solution of **SPA** (80 μM) shows strong absorption bands at 288 nm – 430 nm and 430 nm – 630 nm in the UV-vis absorption spectrum (Figure 2a, black-line and Table S1), indicating a mixture of *open*-isomer (**SPA$_{Open}$**) and *closed*-isomer (**SPA$_{Closed}$**). The methanol solution of **SPA** (80 μM) was irradiated with 505 nm cyan-light at 20 °C for 1 min (Figure 2a, orange-line), and then reached photostationary state (PSS, Figure 2a, red-line). The decreased of absorbance was observed at 430 nm – 630 nm (Figure 2a, red-line and Figure S1c, red-area). Subsequently, the solution was further irradiated with 365 nm UV-light (20 °C, 1 min). The increased absorbance at 430 nm – 630 nm

(Figure S1a, blue-line and Figure S1c, blue-area), revealing a partial reverse photoisomerization process from **SPA$_{Closed}$** to **SPA$_{Open}$**. The photoisomerization process between **SPA$_{Closed}$** and **SPA$_{Open}$** driven by sequential 365 nm UV-light and 505 nm cyan-light irradiation (20 °C, 1 min) could be repeated over 6 cycles with limited sign of fatigue (Figure S1b). Furthermore, the PSS of both **SPA$_{Open}$** and **SPA$_{Closed}$** were demonstrated with good photostabilities even prolonged photoirradiation time extended to 180 min (Figure S2a–S2d). Spiropyran switches are not only driven by UV-light, but also driven by thermal back process for switching between their *closed*-isomer and *open*-isomer in protic solvent, due to the stabilized ground state of the *open*-isomer through hydrogen bond interaction.[38,39] To monitor the photoisomerization followed by thermal back processes of **SPA**, UV-vis and ^{1}H nuclear magnetic resonance (NMR) were employed. A methanol solution of **SPA** (80 μM) was irradiated with 505 nm cyan-light irradiation to induce identical photoisomerization process from **SPA$_{Open}$** to **SPA$_{Closed}$** (Figure S2e, red-line) to that of observed in Figure 2a. Subsequently, the solution was heated to 60 °C and observed with an increased absorbance was observed at 288 nm – 630 nm with subtle red-shift (Figure 2b, cyan-line). Upon cooling the solution from 60 °C to 20 °C for 6 min, a subtle blue-shift was observed with absorption maximum at 530 nm (Figure 2b, blue-line). Besides, clear isosbestic points at 326 nm and 344 nm were observed, indicating the thermal back process from **SPA$_{Closed}$** to **SPA$_{Open}$**. The photoisomerization followed by thermal back processes of **SPA**, driven by sequential 505 nm cyan-light irradiation (20 °C, 1 min), heating (60 °C, 25 min) and cooling process (20 °C, 6 min), it can be repeated over six cycles without significant sign of fatigue (Figure 2c). ^{1}H NMR spectral shifts were observed in selected aliphatic regions, upon irradiation of 505 nm cyan-light for 60 min and heating at 60 °C subsequently for 180 min (Figure S3a-S3c). A CD_3OD solution of **SPA** (6.1 mM) shows a mixture of **SPA$_{Closed}$** and **SPA$_{Open}$** with a ratio of **SPA$_{Closed}$** : **SPA$_{Open}$** 1 : 1

(Figure S3a). Upon 505 nm cyan-light irradiation (20 °C, 60 min), the singlet proton at δ = 1.81 ppm was diminished. The mixture of **SPA$_{Open}$**/**SPA$_{Closed}$** was completely isomerized to **SPA$_{Closed}$**, indicating a 505 nm cyan-light induced isomerization process from **SPA$_{Open}$** to **SPA$_{Closed}$** (Figure S3b). Subsequently, the resulting **SPA$_{Closed}$** solution was heated at 60 °C for 180 min (Figure S3c). The singlet protons at δ = 1.18 ppm and 1.26 ppm were downfield-shifted to δ = 1.81 ppm. The isomerization ratio driven by heating at 60 °C was determined as 55:45 (**SPA$_{Closed}$** : **SPA$_{Open}$**). The results from UV-vis absorption and ^{1}H NMR studies indicated the feasibility of the photoisomerization followed by thermal back processes of **SPA** in organic media, even in the presence of anionic charged end-group of the **SPA** molecular design.

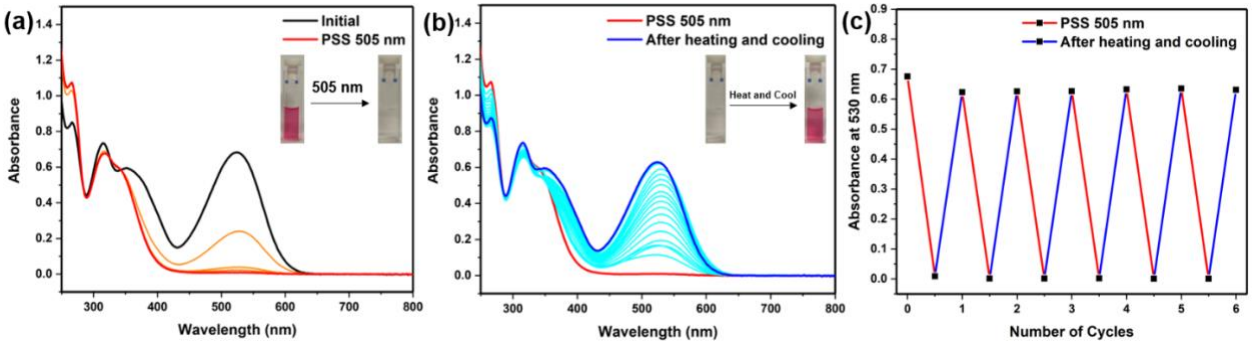

Figure 2. UV-vis absorption spectra of **SPA** in MeOH (80 μM), (a) irradiation of 505 nm cyan-light for 1 min from **SPA$_{Open}$** to **SPA$_{Closed}$**. (b) thermal back and cooling process for 31 min from **SPA$_{Closeed}$** to **SPA$_{Open}$**. (c) Multiple photo/thermal back cycles of **SPA**. Irradiation of UV-vis sample was carried out at 20 °C using Thorlabs model M505L4-C1 high-power LED (505 nm, 1.0 A).

The thermal back processes of **SPA** after photoisomerization were also investigated with UV-vis spectroscopy. Given that spiropyran motif is sensitive to pH environment, it can be deprotonated or protonated its *open*-isomer in aqueous media by a base or acid. Our investigation

has been started from estimating the pK_a values of **SPA** in aqueous media. **SPA** was directly dissolved in MilliQ water (1 mg/mL), followed by diluting **SPA** into 80 μM with 0.5 M HCl or NaOH accordingly to obtain **SPA** solutions with a range of pH 2–11, which the sulphate group of **SPA** should remain negatively charged. UV-vis spectra of **SPA$_{Open}$** (below pH 5) were acquired after heated at 60 °C for 40 min and sequentially cooled at 20 °C for 15 min (Figure S4a–S4c). The strong absorption band at 257 nm – 630 nm with an absorption maximum at 416 nm was observed, indicating the formation of protonated *open*-isomer, *i.e.*, protonated merocyanine (**MCH**$^+$) of **SPA** (Figure S5a, blue-line). While increasing the pH values (above pH 5), a strong absorption band at 257 nm – 630 nm with a new absorption maximum peak at 497 nm, indicating the formation of deprotonated *open*-isomer, *i.e.*, merocyanine (**MC**) of **SPA** (Figure S4d-S4i and Figure S5a, red-line). The p$K_a^{Thermal}$ of **SPA** was estimated by fitting the profiles of the absorbance peak at 497 nm of both **MCH**$^+$ and **MC** forms against pH values into a non-linear least-squares curve fitting to the Boltzmann equation, the detail of the calculation was discussed in the supporting information. The resulting p$K_a^{Thermal}$ was calculated as 4.71 ± 0.12 (Figure S5b), revealing that aqueous solutions of **SPA** can be deprotonated above pH 5 with good aqueous solubility. Furthermore, an aqueous solution of **SPA** was prepared as 5.0 wt.% by dissolving in MilliQ water with pH tuning, followed with annealing process by heating (60 °C, 20 min) and cooling (20 °C) to afford a deep red solution. An aqueous solution of **SPA** (80 μM, pH 9.0, 20 °C) showed a broad and strong absorption band at 254 nm – 630 nm with an absorption maximum at 497 nm and accompanied with two shoulder peaks at 386 nm and 316 nm, respectively (Figure 3a, black-line), with an obvious hypsochromic-shift of ~ 33 nm of the absorption maximum than that in methanol solution (Figure 2a). Upon 505 nm cyan-light irradiation, the strong absorption band at 293 nm – 630 nm was decreased with a bathochromic-shift and an isosbestic point at 293 nm,

revealing the photoisomerization process from **SPA$_{Open}$** to **SPA$_{Closed}$** and negative solvatochromism property (Figure 3a, red-line and Figure S6, red-area). Subsequently, the resulting solution was heated to 60 °C for 40 min and cooled for 15 min, in showing a thermal back process from **SPA$_{Closed}$** to **SPA$_{Open}$** with a hypsochromic-shift. (Figure 3a, blue-line and Figure S6, blue-area). When the second switching cycle was performed with 505 nm cyan-light irradiation, after thermal back process to **SPA$_{Open}$** in the first cycle, it can switch completely back to **SPA$_{Closed}$** with the diminishment of the maxima peak at 497 nm, possibly due to complete dissolution of the aggregates after a series of heating processes (Figure 3c and Figure S7a, red-line). Subsequently, the photoisomerization followed by thermal back processes of **SPA** cycles in aqueous medium were performed (Figure S7b, blue-line) and repeated by alternatively 505 nm cyan-light irradiation and thermal back (60 °C) and cooling process (20 °C) for 4 cycles with sign of fatigue (Figure 3c). To further verify the photo/thermal stability of **SPA** in aqueous media, an aqueous solution of **SPA** (80 μM, pH 9.0) was irradiated with 505 nm cyan-light, which the irradiation duration was extended from 1 min to 180 min (Figure S7c–S7d), showing that absorption band at 293 nm – 630 nm can be further reduced and remained stable after 80 min photoirradiation. The obtained solution of **SPA** was further heated at 60 °C for 1000 min (Figure S7e–S7f), which was 25 times extended heating process. In the initial 40 min of heating process, the thermal back process proceeded smoothly to reach PSS, however, significant decrease of absorption band at 430 nm – 600 nm was observed upon prolonged heating to 1000 min, indicating that the PSS of **SPA$_{Open}$** became instable upon prolonged heating. The extended thermal back processes of **SPA** should be attributed for the sign of fatigue as observed in Figure 3c.

With the advantage of broad absorption spectrum ranged at 293 nm – 630 nm, photoirradiation of an aqueous solution of **SPA** was able to perform with slightly red-shifted 530 nm green-light LED. Upon 530 nm green-light irradiation for 1 min, the strong absorption band at 293 nm – 630 nm was able to induce identical photoisomerization from **SPA$_{Open}$** to **SPA$_{Closed}$** (Figure S8a, red-line and Figure S8d, red-area). Subsequently, the solution was performed thermal back at 60 °C for 40 min and cooling process at 20 °C for 15 min to show a thermal back process from **SPA$_{Closed}$** to **SPA$_{Open}$** (Figure S8b, blue-line and Figure S8d). The switching cycle could perform 4 times by photoirradiation and thermal back reaction with similar fatigue signs (Figure S8c) to that Figure 3c. The results showed the feasibility of the photoisomerization /thermal back of **SPA**, in this connection, supramolecular transformations can be induced by photo and thermal stimulated processes in aqueous media.

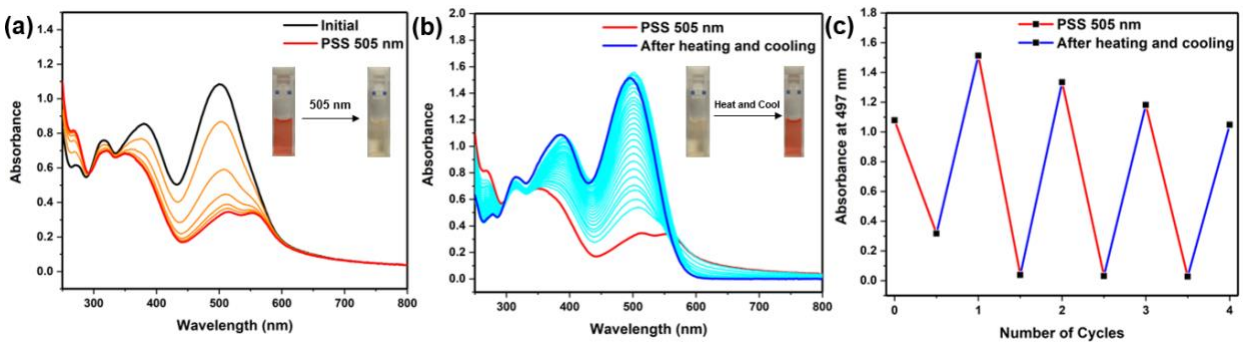

Figure 3. UV-vis absorption spectra of **SPA** in MilliQ water (80 μM, pH 9.0), (a) irradiation of 505 nm cyan-light for 1 min from **SPA$_{Open}$** to **SPA$_{Closed}$**. (b) thermal back and cooling process for 55 min from **SPA$_{Closed}$** to **SPA$_{Open}$**. (c) Multiple photo/thermal back cycles of **SPA**. Irradiation of UV-vis sample was carried out at 20 °C using Thorlabs model M505L4-C1 high-power LED (505 nm, 1.0 A).

2.2. Microscopic Supramolecular Transformations of SPA in Aqueous Media

A freshly prepared aqueous solution of **SPA** (74.1 mM, 5.0 wt.%, pH 9.0) in presence of 1.0 equivalent of NaOH was diluted into a range of the concentration from 1.0 x 10^{-4} to 1.0 mM for estimating the critical aggregation concentration (CAC) of **SPA** by using pyrene fluorescence assay, which the pyrene aggregates into the hydrophobic environment of the supramolecular assemblies. A significant drop of I_1/I_3 ratio was observed to reveal that pyrene aggregates into a more hydrophobic environment and incorporates into the hydrophobic supramolecular assemblies. The CAC of aqueous solutions of $\mathbf{SPA_{Open}}$ and $\mathbf{SPA_{Closed}}$ was estimated as < 19 μM and < 88 μM, respectively (Figure S9a and S9b). It is noted that the concentration of **SPA** in the UV-vis spectroscopic analysis was above the CAC (Figure 3a, red-line). To further investigate the photoisomerization followed by thermal back processes of **SPA** in supramolecular assembled states at microscopic length-scale, a freshly prepared 0.3 wt.% solution of **SPA** (4.7 mM, pH 9.0) was imaged with negative-stained transmission electron microscopy (TEM), showing worm-like micelles (Figure S10). Cryogenic transmission electron microscopy (cryo-TEM) was employed for imaging nanostructures of **SPA**, in avoiding significant drying effect in TEM studies. Worm-like micelles nanostructure with ~ 5.7 nm in diameter and micrometers in length were observed (Figure 4a) with major component of $\mathbf{SPA_{Open}}$ (1.0 wt.%, 14.8 mM), indicating that the zwitterionic-form of spiropyran connected with negatively charged sulphate motif can be stabilized in aqueous media to form supramolecular structure, which can facilitate the fabrication of macroscopic soft scaffolds. Head-to-head arrangement of $\mathbf{SPA_{Open}}$ should be formed with minimized dipolar moment of the resulting worm-like micelles nanostructure, even with lower concentration of $\mathbf{SPA_{Open}}$ (0.7 wt.%, 10.4 mM, Figure S11a). Upon 505 nm cyan-light irradiation (20 °C, 60 min), the large aspect-ratio nanostructures of $\mathbf{SPA_{Open}}$ were transformed into a mixture of supramolecular lamellar structures and small portion of worm-like micellar structures (Figure

4b and Figure S11b), indicating significant increase of packing parameters upon photoisomerization from **SPA**$_{\mathbf{Open}}$ to **SPA**$_{\mathbf{Closed}}$ with tighter packing of non-charged form of spiropyran units. The obtained solution, after photoirradiation, was heated at 60 °C for 60 min and cooled to afford partially reformed the supramolecular worm-like micelles with shorter length of the nanostructure (Figure 4c and Figure S11c). Though significant drying effect was observed in TEM images for the photoisomerization followed by thermal back processes of **SPA** in aqueous media (Figure S12a and S12b). The results observed in TEM and cryo-TEM studies indicated that the photoisomerization followed by thermal back processes of **SPA** in aqueous media can reversibly control the supramolecular transformations of **SPA**.

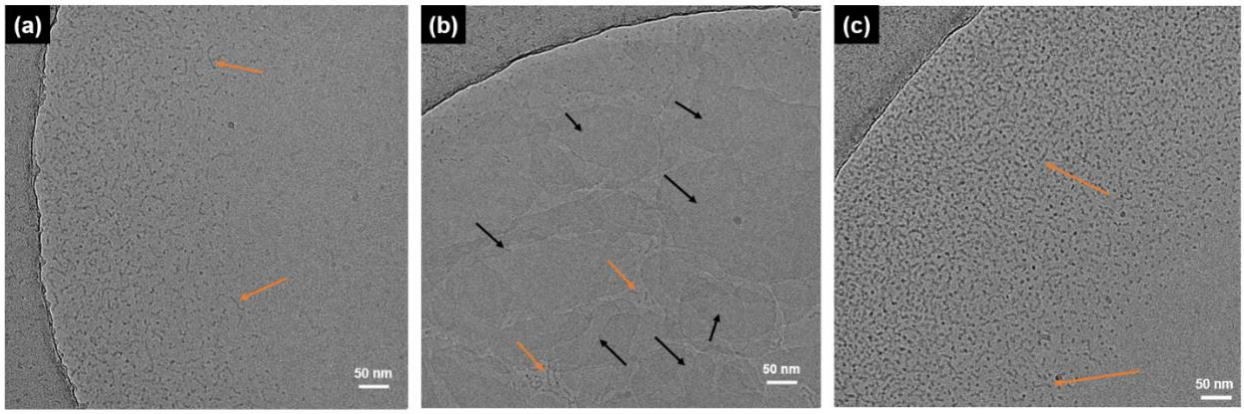

Figure 4. Cryo-TEM images of 1.0 wt.% **SPA** (14.8 mM, pH 9.0) diluted from annealed 5.0 wt.% **SPA**. (a) before irradiation (orange-arrows: worm-like micelles), (b) after 505 nm photoirradiation for 60 min (orange-arrows: worm-like micelles nanostructures; black-arrows lamellar nanostructures) and (c) after thermal back at 60 °C for 60 min (orange-arrows: worm-like micelles).

2.3. Structural Properties and Macroscopic Actuation Mechanism of Supramolecular Soft Scaffolds of SPA

A freshly prepared aqueous solution of **SPA** (74.1 mM, 5.0 wt.%, pH 9.0), in the presence of 1.0 equivalent of NaOH, was ejected into a shallow-pool of calcium chloride solution (150 mM) with a shear-flow method, in affording a hydrogel-like material, *i.e.*, macroscopic soft scaffold (Figure S13), but low structural stability of the obtained scaffold was observed, due to slow scaffold stabilization. In considering the sulphate group of **SPA** cannot be effectively charged screened with divalent cations, non-colored trivalent cation, *i.e.*, scandium chloride ($ScCl_3$), with higher charge density, low biotoxicity, and stability in aqueous media, can serve to stabilize macroscopic soft scaffold of **SPA**.[29] To increase the macroscopic soft scaffold stability, a solution of **SPA** (74.1 mM, 5.0 wt.%, pH 9.0) was ejected into a scandium chloride solution (150 mM) to give a stable macroscopic soft scaffold with ~300 μm in diameter (Figure 5a, Figure S14 and Movie S1). The scaffold of **SPA** was imaged under optical microscopy (OM) with or without polarizer, showing limited birefringence with subtle unidirectional alignment of the supramolecular worm-like micelles nanostructure (Figure S15). A stable macroscopic soft scaffold of **SPA** was prepared with identical method in a capillary tube, which was immersed in scandium chloride solution (150 mM). The **SPA** scaffold was ejected into the capillary tube and sealed to maintain stable humidity during X-ray exposure when applying through-view small-angle X-ray scattering (SAXS) setup. The 2D-SAXS image of **SPA** scaffold does not exhibit any directional scattering at the region of $q = 0.1 – 0.45$ nm^{-1} (Figure S16a). After converting the 2D-SAXS image of the **SPA** scaffold to 1D-SAXS pattern, it showed with a diffraction peak with *d*-spacing of 2.56 nm (Figure 5b). The diffraction peak is derived from the head-to-head arrangement of **SPA$_{Open}$**. Additionally, when employing through-view wide-angle X-ray diffraction (WAXD), the 2D-WAXD image of the **SPA** scaffold showed no evidence of directional diffraction (Figure S16b). The converted 2D-WAXD image to 1D-WAXD pattern of the **SPA** scaffold reveals a diffraction

peak with *d*-spacing of 2.58 nm, which it also arises from the head-to-head arrangement of **SPA$_{Open}$** (Figure S16c), and the *d*-spacing of 0.37 nm is representing weak π-π interactions of **SPA$_{Open}$**.

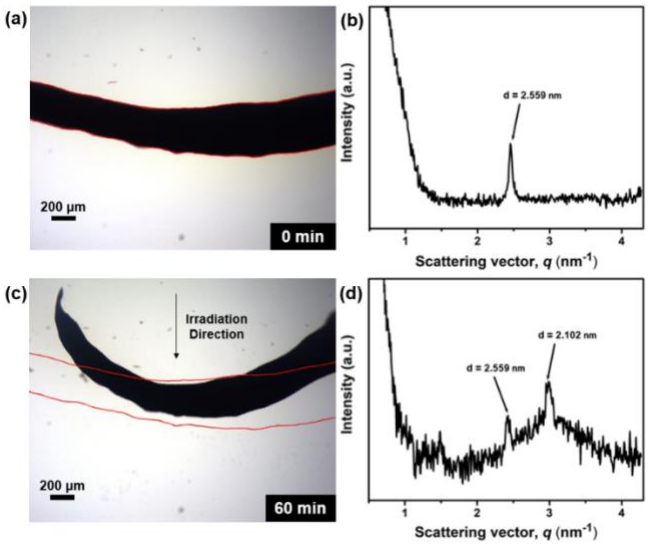

Figure 5. Snapshots of photoactuation of macroscopic soft scaffold of **SPA** (5.0 wt.%, pH 9.0, 74.1 mM) in $ScCl_3$ (150 mM) (a) before and (c) after irradiation with 505 nm cyan-light for 60 min. The macroscopic soft scaffold of **SPA** bends towards the cyan-light source. 1D-SAXS pattern of a macroscopic soft scaffold of **SPA** (5.0 wt.%, pH 9.0, 74.1 mM) (b) before and (d) after 505 nm cyan-light irradiation, showing the diffraction pattern perpendicular to the long axis of the scaffold.

With elucidated structural details of **SPA** scaffold, upon 505 nm cyan-light irradiation (20 °C, 60 min) was applied to one-side of the scaffold with a distance of 5.0 cm, the **SPA** scaffold was bent toward the light source with low flexion angle (48°) and slow actuation speed (0.8 °/min, Figure 5c and Movie S2). To provide structural details of the photoactuated scaffold, a **SPA** scaffold, prepared with identical method, was irradiated with 505 nm cyan-light irradiation (20 °C, 60 min) to one-side of the scaffold in a capillary tube and subsequently measured with SAXS. The

2D-SAXS image of photoirradiated **SPA** scaffold shows consistently no sign of directional scattering in the region of $q = 0.1 – 0.45$ nm^{-1} (Figure S17c), while a pair of diffraction peaks with *d*-spacings of 2.56 nm and 2.10 nm was revealed in the 1D-SAXS pattern (Figure 5d). The results indicated that a closer-packed head-to-head arrangement of **SPA$_{Closed}$** was observed upon partial photoisomerization from **SPA$_{Open}$** to **SPA$_{Closed}$**, and hence both diffractions originated from head-to-head arrangements of **SPA$_{Open}$** (2.56 nm) and **SPA$_{Closed}$** (2.10 nm) were revealed, respectively. The mixed assemblies packing structures of both **SPA$_{Open}$** and **SPA$_{Closed}$** significantly reduced the structural order upon photoisomerization with 505 nm cyan-light irradiation, as revealed with decreased signal-to-noise ratio in Figure 5d. The 2D-WAXD image of photoirradiated **SPA** scaffold shows no significant sign of directional diffraction (Figure S17b), while the converted 1D-WAXD pattern shows a consistence observation of a closer-packing head-to-head arrangement of **SPA$_{Closed}$** with *d*-spacing of 2.10 nm diffraction peak (Figure S17c).

To examine the macroscopic soft scaffold expulsion of water induced by the photoisomerization process, a **SPA** scaffold, prepared with the identical method, was removed all surrounding aqueous solution and replaced with dodecane (Figure S18a). Photoirradiation of 505 nm cyan-light was applied with a distance of 5 cm (20 °C, 60 min), the scaffold was ejecting water to the immiscible dodecane (Figure S18b and Movie S3), while the scaffold was slightly bending toward light source with partial shrinking (Figure S18c). The microscopic supramolecular transformation, as a result of photoisomerization, from worm-like micelles nanostructure to a mixture of supramolecular lamellar structure and small portion of worm-like micelles nanostructure was induced by increased packing density of head-to-head arrangements of **SPA** units, as confirmed with XRD studies. The relatively large aspect-ratio worm-like micelles nanostructure of **SPA$_{Open}$** with zwitterionic nature

can entrap water efficiently upon macroscopic soft scaffold formation. Upon photoisomerization, the supramolecular lamellar structures of $\mathbf{SPA_{Closed}}$ cannot retain entrapped water after isomerized to non-charged spiropyran motifs. Considering the light-penetration difference to the scaffold with ~ 240 μm in thickness, the photoirradiated side of the **SPA** scaffold shows predominant loss of water than non-irradiated side of the scaffold, and resultingly, macroscopic contraction on the photoirradiated side is faster than non-irradiated side to offer macroscopic actuations. While a macroscopic soft scaffold of **SPA** (3.0 wt.%, pH 9.0) in aqueous solution of $ScCl_3$ (150 mM) was isotropic shrinking upon irradiation with green-light laser pointer at both left and right sides for 2 min (Figure S19 and Movie S4). The results indicated the photoactuation motions occurred evenly on both sides of the scaffold. Besides, both shorter and longer axis of the scaffold were shrinking, revealing that the total volume of the scaffold was reduced after water expulsion. An annealed aqueous solution of 5.0 wt.% **SPA** was mixed with a FluoSpheres™ Polystyrene Microspheres suspension at 3:2 volumetric ratio to obtain a 3.0 wt.% aqueous solution of **SPA** as a final concentration. The macroscopic soft scaffold of **SPA** encapsulated microspheres and bent toward the 530 nm green-light laser pointer upon irradiation, the microspheres was moved as following the macroscopic actuation movement of the **SPA** scaffold without any observable leakage of microspheres (Figure S20a and S20c, Movie S5). It is noted that a particular encapsulated microspheres in the **SPA** scaffold was selected and highlighted in Figure S20 to monitor through the actuation movement of the **SPA** scaffold. The distance between the microsphere and the left edge of the **SPA** scaffold was measured as 17 μm (Figure S20b). After irradiated with 530 nm green-light laser pointer for 7 s, the distance between microsphere and the left edge of the scaffold **SPA** was slightly decreased to 7 μm (Figure S20d). The results indicated that the particular microsphere was moved toward the left edge of the scaffold **SPA,** due to light penetration

difference from the left edge to right edge of the scaffold. AFM was performed to analyze the mechanical properties and mechanism of the actuation function of macroscopic soft scaffold of **SPA** in 3.0 wt.%. The stiffness of the macroscopic soft scaffold **SPA** before irradiation and after green-light laser irradiation for 1 min were measured with the Young modulus of 463.7 ± 270.4 kPa and 608.0 ± 329.5 kPa, respectively (Figure S21). The results suggested that the macroscopic actuation function of macroscopic soft scaffold **SPA** was accompanied by photoirradation and water expulsion, which caused the density of macroscopic soft scaffold increased to afford a harder material surface.

In combination of all results obtained from molecular level, nanoassembly level, and to macroscopic level, the photoactuation mechanism of **SPA** scaffolds can be systematically concluded. The important molecular design of **SPA** in *Open*-isomer form enables highly charged nature without loss of supramolecular assembly propensity in aqueous media, in forming nanoassembly (worm-like micelles). Upon photoisomerization of **SPA** driven by either cyan-light or green-light, the significant molecular geometrical transformation from $\mathbf{SPA_{Open}}$ to $\mathbf{SPA_{Closed}}$ can be smoothly controlled under neutral and basic pH, while nanoassembly (worm-like micelles) of $\mathbf{SPA_{Open}}$ with highly charged zwitterionic structure can be transformed efficiently into lamellar structures of $\mathbf{SPA_{Closed}}$, which have been clearly validated with UV-vis spectroscopic and electron microscopic measurements (Figures 2–4). It is clearly demonstrated that the tight correlation between molecular motion and supramolecular assembly transformation at microscopic length-scale, in converting photo-energy to molecular motions and even inducing nanoassembly structural transformation through molecular motion accumulated upon photoisomerization. The highly negative charged surface of nanoassembly (worm-like micelles) of $\mathbf{SPA_{Open}}$ can be effectively

charged screened with trivalent cation scandium for stabilizing and forming macroscopic soft scaffold of **SPA**. It is noted that the highly charged nature of nanoassembly of **SPA** within the macroscopic soft scaffold facilitates a better water entrapment, in affording the scaffold with 5.0 wt.% of material and 95 wt.% of water. The nanoassembly of $\mathbf{SPA_{Open}}$ was packed in the scaffolds randomly without significant structural alignment (Figures 5 and S16), while both nanoassembly (worm-like micelles) of $\mathbf{SPA_{Open}}$ and lamellar structures of $\mathbf{SPA_{Closed}}$ were coexisted in the scaffold. Significant selective shrinkage of **SPA** scaffolds, upon photoirradiation, induced macroscopic actuation (Figures 5 and S20), as a result of entrapped water release from the scaffold (Figure S18) due to significant loss of highly charged nanoassembly of $\mathbf{SPA_{Open}}$. Besides, the shrinkage of **SPA** scaffolds was accompanied with increased material density (Figure S21). The macroscopic actuation mechanism of **SPA** scaffolds was clearly demonstrated energy conversion from photo-energy to molecular motions, induced nanostructures transformation for releasing entrapped water, and amplification of motions to macroscopic actuation.

2.4. Macroscopic Actuations of Supramolecular Macroscopic Soft Scaffolds of SPA and Related Cytocompatibility

With the interpretated macroscopic actuation mechanism of **SPA**, a series of macroscopic actuation studies were performed with fixed optimally distance at 0.5 cm between the light source and **SPA** scaffold in aqueous media. An annealed aqueous solution of **SPA** (5.0 wt.%, pH 9.0, 74.1 mM) was prepared into a macroscopic soft scaffold in a glass container and performed macroscopic actuation experiment by irradiating with 505 nm cyan-light (Figure 6a and Movie S6), showing 90° flexion angle at 10 min with a faster actuation speed 9.0 ± 0.14 °/min than that Figure 4A under microscope. A lower concentration of **SPA** in 3.0 wt.% (44.5 mM) and 1.0 wt.%

(14.8 mM) showed faster macroscopic actuation speeds driven by 505 nm cyan-light with actuation speed of 21.8 ± 0.94 °/min (Figure 6b and Movie S7a) and 27.7 ± 1.56 °/min (Figure 6c and Movie S8), respectively. It is noted that the **SPA** scaffold color was changed from red to yellow color (Figure 5c), indicating the photoisomerization process from $\mathbf{SPA_{Open}}$ to $\mathbf{SPA_{Closed}}$. The faster macroscopic actuation speed was observed with lower concentration of the macroscopic soft scaffolds of **SPA**, due to lower structural rigidity and effective light penetration for photoisomerization from $\mathbf{SPA_{Open}}$ to $\mathbf{SPA_{Closed}}$ within the macroscopic scaffolds. With the demonstrated photoactuation process of **SPA** scaffolds, the thermal back process of **SPA** scaffolds (3.0 wt.%, 44.5 mM) was investigated after photoactuation with 505 nm cyan-light to attain 78° flexion angle (Figure S22a). The pale-yellow actuated scaffold of **SPA** was observed under a temperature-controlled reflected light microscopy with a preheated stage at 60 °C over 30 min. The pale-yellow scaffold was turned red in color immediately, due to thermal induced transformation from $\mathbf{SPA_{Closed}}$ to $\mathbf{SPA_{Open}}$ (Figure S22b). The scaffold was reversely bent within 5 min with significant shrinkage in length from ~1.9 cm to ~0.9 cm, it is possibly attributed to the instable macroscopic scaffold of **SPA** upon heating at 60 °C to reduce capability in water entrapment (Figure S22b, Movie S7b), instead of thermal back process of **SPA**. As macroscopic soft scaffold of **SPA** in 3.0 wt.% can afford a relatively stable macroscopic and faster macroscopic actuation, a more powerful light source of 530 nm green-light laser pointer was applied to demonstrate faster macroscopic actuation speeds. Given that a macroscopic soft scaffold of 3.0 wt.% **SPA** was fabricated in $ScCl_3$ (150 mM) and subjected to another wavelength of LED light irradiation (530 nm green-light), a slower macroscopic actuation speed of 9.0 °/min was observed in comparing to 505 nm LED cyan-light irradiation (Figure S23 and Movie S9), due to the lower molar absorptivity of **SPA** at 530 nm wavelength (Figure 3b, black-line). A more powerful light

source of 530 nm green-light laser pointer was applied to demonstrate a faster macroscopic actuation. A macroscopic scaffold of 3.0 wt.% **SPA** was fabricated in $ScCl_3$ (150 mM) and subjected to 530 nm green-light laser pointer with a distance of 1.5 cm between the light source and scaffold, the fastest macroscopic actuation speed was observed with 83.4 ± 5.27 °/min (Figure 7a and Movie S10), which is nine times faster than that of observed for 530 nm LED green-light irradiation (Figure S23). Besides, a multiple-points actuation experiment of macroscopic soft scaffold of **SPA** was demonstrated with 530 nm green-light laser pointer, the **SPA** scaffold was irradiated alternatively from left to right side each for 60 s to form a zigzag shaped macroscopic soft scaffold of **SPA** (Figure 7b and Movie S11), indicating the potential feasibility of precise robotic functions. Photoactuation experiments with different light sources, concentration effect of **SPA**, and thermal back processes, have clearly demonstrated the high reproducibility of photoactuation processes of **SPA** scaffolds for potential practical applications of soft robotics.

Besides, a cytocompatibility of **SPA** was examined to evaluate potential cytotoxicity of the nanostructures of **SPA**. A MTS assay was applied to determine the cell viability of human bone marrow-derived mesenchymal stem cells (hBM-MSCs) with the aqueous solution of **SPA** in the concentration rage of 1 to 100 μM with a control sample (Figure S24), which the hBM-MSCs has been widely demonstrated with controllable differentiations and clinical translations. The results showed that a high cell viability (> 70%) was observed after incubation hBM-MSCs with aqueous solution of **SPA** in the concentration range of 1 to 100 μM over 4 days. The good cytocompatibility observed in hBM-MSCs.

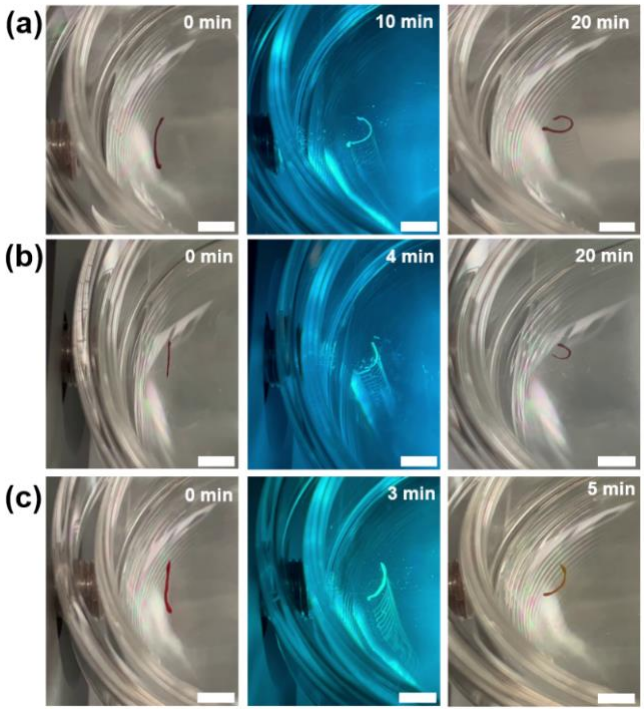

Figure 6. (a) Images of the macroscopic soft scaffold of **SPA** (5.0 wt.%, pH 9.0, 74.1 mM) and (b) macroscopic soft scaffold of **SPA** (3.0 wt.%, pH 9.0, 44.5 mM) in $ScCl_3$ (150 mM), and following with 20 minutes photoirradiation of 505 nm cyan-light from the left side. (c) Images of the macroscopic soft scaffold of **SPA** (1.0 wt.%, pH 9.0, 14.8 mM) in $ScCl_3$ (150 mM) and following with 5 minutes photoirradiation of 505 nm cyan-light from the left side. The distance between the light source and the macroscopic soft scaffold in all demonstrations is 0.5 cm. Scale bars for all panels: 0.5 cm.

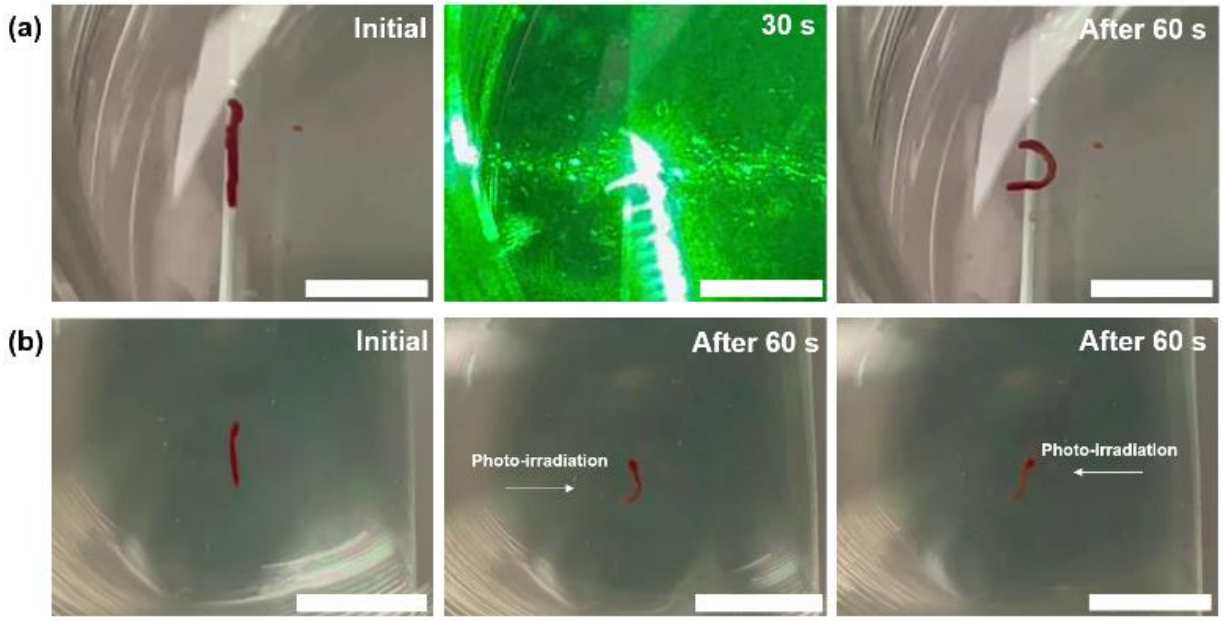

Figure 7. (a) Snapshots of macroscopic soft scaffold of **SPA** (3.0 wt.%) in $ScCl_3$ (150 mM) after irradiation with 530 nm green-light laser pointer from left side for 60 s. (b) Snapshots of macroscopic soft scaffold of **SPA** (3.0 wt.%) in $ScCl_3$ (150 mM) after alternatively irradiation with 530 nm green-light laser pointer from left to right side each for 60 s, resulting in zigzag conformation. Scale bars for all panels are 0.5 cm.

3. Conclusion

Spiropyran amphiphile, functionalized with a negative charged sulfonated end-group, was synthesized with confirmation through NMR spectroscopies (Figure S25-S28).and high resolution of electrospray ionization quadrupole-time-of-flight Mass spectrometry (Figure S29-S30) and designed for fabrications of macroscopic soft scaffolds. The excellent photoswitchability in both organic and aqueous media has been confirmed by UV-vis absorption and NMR spectroscopies. Optimization of pH value with maximized *open*-isomer of **SPA**, highly charged supramolecular nanostructures were formed with effective and dynamic supramolecular transformations upon cyan-light irradiation followed with a thermal back process. Highly charged nanostructures of **SPA**

have been enabled to form mechanically stable macroscopic soft scaffold in the presence of scandium ions. Upon green/cyan-light irradiation, the macroscopic soft scaffolds bent towards the light source induced by water expulsion, with the fastest macroscopic actuation speed of 83.4 ± 5.27 °/min. Detailed supramolecular nanoassembly processes and macroscopic actuation mechanism in aqueous media have been confirmed with X-ray diffraction, atomic force microscopy and electron microscopic studies. The current research approach has laid the foundation for the new generation of supramolecular soft robotics without high structural requirements, in sustaining soft actuating robotic functions. It could open up new prospects toward development of future soft robotic nanomaterial systems.

ASSOCIATED CONTENT

The following files are available free of charge.

Materials used in this work; synthetic details; material characterization; experimental details; and data not included in the main text (PDF)

Movie S1, Preparation of a macroscopic soft scaffold **SPA** (5.0 wt.%) in $ScCl_3$ (MP4)

Movie S2, Photoactuation of a macroscopic soft scaffold **SPA** (5.0 wt.%) in $ScCl_3$ under microscope after photoirradiation of 505 nm cyan-light from top side at a distance of 5 cm (MP4)

Movie S3, Photoirradiation of a macroscopic soft scaffold of **SPA** (5.0 wt.%) immersed in dodecane after photoirradiation of 505 nm cyan-light from left side at a distance of 5 cm (MP4)

Movie S4: Photoirradiation of a macroscopic soft scaffold **SPA** (3.0 wt.%) in $ScCl_3$ under microscope after photoirradiation of 530 nm green-light laser pointer from both left and right sides at a distance of 5 cm (MP4)

Movie S5, Photoactuation of a macroscopic soft scaffold **SPA** encapsulated FluoSpheres™ Polystyrene Microspheres (3.0 wt.%) in $ScCl_3$ after photoirradiation of 530 nm green-light laser pointer from left at a distance of 5 cm (MP4)

Movie S6, Photoactuation of a macroscopic soft scaffold **SPA** (5.0 wt.%) in $ScCl_3$, after photoirradiation of 505 nm LED cyan-light from left side at a distance of 0.5 cm (MP4)

Movie S7a, Photoactuation of a macroscopic soft scaffold **SPA** (3.0 wt.%) in $ScCl_3$, after photoirradiation of 505 nm LED cyan-light from left side at a distance of 0.5 cm (MP4)

Movie S7b, Photoactuation of a macroscopic soft scaffold **SPA** (3.0 wt.%) in $ScCl_3$, after photoirradiation of 505 nm LED cyan-light from left side at a distance of 0.5 cm and thermal-responsive property (MP4)

Movie S8, Photoactuation of a macroscopic soft scaffold **SPA** (1.0 wt.%) in $ScCl_3$, after photoirradiation of 505 nm LED cyan-light from left side at a distance of 0.5 cm (MP4)

Movie S9, Photoactuation of a macroscopic soft scaffold **SPA** (3.0 wt.%) in $ScCl_3$, after photoirradiation of 530 nm LED green-light from left side at a distance of 0.5 cm (MP4)

Movie S10, Photoactuation of a macroscopic soft scaffold **SPA** (3.0 wt.%) in $ScCl_3$, after photoirradiation of 530 nm green-light laser pointer from left side at a distance of 1.5 cm (MP4)

Movie S11, Photoactuation of a macroscopic soft scaffold **SPA** (3.0 wt.%) in $ScCl_3$, after photoirradiation of 530 nm green-light laser pointer alternatively from left to sides at a distance of 1.5 cm (MP4)

Corresponding Author

Shaoyu Chen - School of Fashion and Textiles, The Hong Kong Polytechnic University, Hong Kong, China. E-mail: shaoyu.chen@polyu.edu.hk

Franco King-Chi Leung - State Key Laboratory of Chemical Biology and Drug Discovery, Research Institute for Future Food, Department of Applied Biology and Chemical Technology, The Hong Kong Polytechnic University, Hong Kong, China E-mail: kingchifranco.leung@polyu.edu.hk

Notes

The authors declare no competing financial interest.

ACKNOWLEDGMENT

This work was supported financially by the Croucher Foundation (Croucher Innovation Award-2021), the Hong Kong Polytechnic University (BC7W, P0046213), the Hong Kong Research Grants Council General Research Fund (GRF 15305822), the Hong Kong Special Administrative Region Government (InnoHK) and the Centre for Eye and Vision Research (CEVR) for F.K.-C. Leung; JSPS KAKENHI (JP21K04877) and the CREST, Japan Science and Technology Agency (JPMJCR23L2) for T. Kajitani. We acknowledge the technical support from UCEA and ULS of PolyU. All authors sincerely appreciate Prof. Dr. Takanori Fukushima (Laboratory for Chemistry and Life Science, Institute of Integrated Research, Institute of Science Tokyo) for his helpful suggestions and generous support in X-ray diffraction analysis.

REFERENCES

(1) Vale, R. D.; Milligan, R. A. The Way Things Move: Looking Under the Hood of Molecular Motor Proteins. *Science* **2000**, *288* (5463), 88–95. https://doi.org/10.1126/science.288.5463.88.

(2) Alberts, B. The Cell as a Collection of Protein Machines: Preparing the Next Generation of

Molecular Biologists. *Cell* **1998**, *92* (3), 291–294. https://doi.org/10.1016/S0092-8674(00)80922-8.

(3) Rayment, I.; Holden, H. M.; Whittaker, M.; Yohn, C. B.; Lorenz, M.; Holmes, K. C.; Milligan, R. A. Structure of the Actin-Myosin Complex and Its Implications for Muscle Contraction. *Science* **1993**, *261* (5117), 58–65. https://doi.org/10.1126/SCIENCE.8316858.

(4) Ebashi, S.; Endo, M. Calcium and Muscle Contraction. *Prog. Biophys. Mol. Biol.* **1968**, *18* (C), 123–183. https://doi.org/10.1016/0079-6107(68)90023-0.

(5) Pilz Da Cunha, M.; Debije, M. G.; Schenning, A. P. H. J. Bioinspired Light-Driven Soft Robots Based on Liquid Crystal Polymers. *Chem. Soc. Rev.* **2020**, *49* (18), 6568–6578. https://doi.org/10.1039/D0CS00363H.

(6) White, T. J.; Broer, D. J. Programmable and Adaptive Mechanics with Liquid Crystal Polymer Networks and Elastomers. *Nat. Mater.* **2015**, *14* (11), 1087–1098. https://doi.org/10.1038/nmat4433.

(7) Xiao, Y.-Y.; Jiang, Z.-C.; Zhao, Y. Liquid Crystal Polymer-Based Soft Robots. *Adv. Intell. Syst.* **2020**, *2* (12), 2000148. https://doi.org/10.1002/AISY.202000148.

(8) Xiao, Y.-Y.; Jiang, Z.-C.; Tong, X.; Zhao, Y. Biomimetic Locomotion of Electrically Powered “Janus” Soft Robots Using a Liquid Crystal Polymer. *Adv. Mater.* **2019**, *31* (36), 1903452. https://doi.org/10.1002/ADMA.201903452.

(9) Yang, X.; Chen, Y.; Zhang, X.; Xue, P.; Lv, P.; Yang, Y.; Wang, L.; Feng, W. Bioinspired Light-Fueled Water-Walking Soft Robots Based on Liquid Crystal Network Actuators with Polymerizable Miniaturized Gold Nanorods. *Nano Today* **2022**, *43*, 101419.

https://doi.org/10.1016/J.NANTOD.2022.101419.

(10) Shintake, J.; Cacucciolo, V.; Floreano, D.; Shea, H. Soft Robotic Grippers. *Adv. Mater.* **2018**, *30* (29), 1707035. https://doi.org/10.1002/ADMA.201707035.

(11) Park, C. S.; Kang, Y. W.; Na, H.; Sun, J. Y. Hydrogels for Bioinspired Soft Robots. *Prog. Polym. Sci.* **2024**, *150*, 101791. https://doi.org/10.1016/J.PROGPOLYMSCI.2024.101791.

(12) Chen, Y.; Zhang, Y.; Li, H.; Shen, J.; Zhang, F.; He, J.; Lin, J.; Wang, B.; Niu, S.; Han, Z.; Guo, Z. Bioinspired Hydrogel Actuator for Soft Robotics: Opportunity and Challenges. *Nano Today* **2023**, *49*, 101764. https://doi.org/10.1016/J.NANTOD.2023.101764.

(13) Goujon, A.; Mariani, G.; Lang, T.; Moulin, E.; Rawiso, M.; Buhler, E.; Giuseppone, N. Controlled Sol-Gel Transitions by Actuating Molecular Machine Based Supramolecular Polymers. *J. Am. Chem. Soc.* **2017**, *139* (13), 4923–4928. https://doi.org/https://doi.org/10.1021/jacs.7b00983.

(14) Benoit, D. S. W.; Schwartz, M. P.; Durney, A. R.; Anseth, K. S. Small Functional Groups for Controlled Differentiation of Hydrogel-Encapsulated Human Mesenchymal Stem Cells. *Nat. Mater.* **2008**, *7* (10), 816–823. https://doi.org/10.1038/nmat2269.

(15) Sano, K.; Ishida, Y.; Aida, T. Synthesis of Anisotropic Hydrogels and Their Applications. *Angew. Chemie Int. Ed.* **2018**, *57* (10), 2532–2543. https://doi.org/10.1002/ANIE.201708196.

(16) Zhao, T.; Tan, Y.; Li, Y.; Wang, X. Ionic Fuel-Powered Hydrogel Actuators for Soft Robotics. *J. Colloid Interface Sci.* **2025**, *677*, 739–749. https://doi.org/10.1016/J.JCIS.2024.08.007.

(17) Arsuffi, B.; Siqueira, G.; Nyström, G.; Titotto, S.; Magrini, T.; Daraio, C. Programmable Multi-Responsive Nanocellulose-Based Hydrogels With Embodied Logic. *Adv. Funct. Mater.* **2024**, *34* (51), 2409864. https://doi.org/10.1002/ADFM.202409864.

(18) Gao, G.; Yin, K.; Han, J.; Hu, Y.; Gu, J.; Wei, J.; Chen, T. Marine Amoebae-Inspired Salting Hydrogels to Reconfigure Anisotropy for Reprogrammable Shape Morphing. *Angew. Chemie Int. Ed.* **2025**, *64* (3), e202416672. https://doi.org/10.1002/ANIE.202416672.

(19) Whitesides, G. M. Soft Robotics. *Angew. Chemie Int. Ed.* **2018**, *57* (16), 4258–4273. https://doi.org/10.1002/ANIE.201800907.

(20) Chau, A. K. H.; Leung, F. K. C. Exploration of Molecular Machines in Supramolecular Soft Robotic Systems. *Adv. Colloid Interface Sci.* **2023**, *315*, 102892. https://doi.org/10.1016/J.CIS.2023.102892.

(21) Li, M.; Pal, A.; Aghakhani, A.; Pena-Francesch, A.; Sitti, M. Soft Actuators for Real-World Applications. *Nat. Rev. Mater.* **2022**, *7* (3), 235–249. https://doi.org/10.1038/s41578-021-00389-7.

(22) Apsite, I.; Salehi, S.; Ionov, L. Materials for Smart Soft Actuator Systems. *Chem. Rev.* **2022**, *122* (1), 1349–1415. https://doi.org/https://doi.org/10.1021/acs.chemrev.1c00453.

(23) Li, C.; Iscen, A.; Sai, H.; Sato, K.; Sather, N. A.; Chin, S. M.; Álvarez, Z.; Palmer, L. C.; Schatz, G. C.; Stupp, S. I. Supramolecular–Covalent Hybrid Polymers for Light-Activated Mechanical Actuation. *Nat. Mater.* **2020**, *19* (8), 900–909. https://doi.org/10.1038/s41563-020-0707-7.

(24) Yang, X.; Shi, W.; Chen, Z.; Du, M.; Xiao, S.; Qu, S.; Li, C. Light-Fueled Nonequilibrium

and Adaptable Hydrogels for Highly Tunable Autonomous Self-Oscillating Functions. *Adv. Funct. Mater.* **2023**, *33* (24), 2214394. https://doi.org/10.1002/ADFM.202214394.

(25) Goulet-Hanssens, A.; Eisenreich, F.; Hecht, S. Enlightening Materials with Photoswitches. *Adv. Mater.* **2020**, *32* (20), 1905966. https://doi.org/10.1002/ADMA.201905966.

(26) Matson, J. B.; Stupp, S. I. Self-Assembling Peptide Scaffolds for Regenerative Medicine. *Chem. Commun.* **2011**, *48* (1), 26–33. https://doi.org/10.1039/C1CC15551B.

(27) Lubbe, A. S.; van Leeuwen, T.; Wezenberg, S. J.; Feringa, B. L. Designing Dynamic Functional Molecular Systems. *Tetrahedron* **2017**, *73* (33), 4837–4848. https://doi.org/10.1016/J.TET.2017.06.049.

(28) Chen, J.; Leung, F. K. C.; Stuart, M. C. A.; Kajitani, T.; Fukushima, T.; Van Der Giessen, E.; Feringa, B. L. Artificial Muscle-like Function from Hierarchical Supramolecular Assembly of Photoresponsive Molecular Motors. *Nat. Chem.* **2018**, *10* (2), 132–138. https://doi.org/10.1038/nchem.2887.

(29) Leung, F. K. C.; Van Den Enk, T.; Kajitani, T.; Chen, J.; Stuart, M. C. A.; Kuipers, J.; Fukushima, T.; Feringa, B. L. Supramolecular Packing and Macroscopic Alignment Controls Actuation Speed in Macroscopic Strings of Molecular Motor Amphiphiles. *J. Am. Chem. Soc.* **2018**, *140* (50), 17724–17733. https://doi.org/https://doi.org/10.1021/jacs.8b10778.

(30) Leung, F. K. C.; Kajitani, T.; A Stuart, M. C.; Fukushima, T.; Feringa, B. L. Dual-Controlled Macroscopic Motions in a Supramolecular Hierarchical Assembly of Motor Amphiphiles. *Angew. Chemie Int. Ed.* **2019**, *58* (32), 10985–10989.

https://doi.org/10.1002/ANIE.201905445.

(31) Chau, M.-H.; Wong, W.-K.; Kajitani, T.; Leung, F. K.-C. Blue Light Controlled Supramolecular Soft Robotics of Phenylazothiazole Amphiphiles for Rapid Macroscopic Actuations. *Adv. Sci.* **2024**, *11* (45), 2407130. https://doi.org/10.1002/ADVS.202407130.

(32) Cheung, L. H.; To, J. C.; Wong, W. K.; Stuart, M. C. A.; Kajitani, T.; Keng, V. W.; Leung, F. K. C. Tailoring Multicontrolled Supramolecular Assemblies of Stiff-Stilbene Amphiphiles into Macroscopic Soft Scaffolds as Cell-Material Interfaces. *ACS Appl. Mater. Interfaces* **2024**, *16* (3), 4056–4070. https://doi.org/https://doi.org/10.1021/acsami.3c16795.

(33) Kwan, K. S. Y.; Lui, Y. Y.; Kajitani, T.; Leung, F. K. C. Aqueous Supramolecular Co-Assembly of Anionic and Cationic Photoresponsive Stiff-Stilbene Amphiphiles. *Macromol. Rapid Commun.* **2022**, *43* (21), 2200438. https://doi.org/10.1002/MARC.202200438.

(34) Cheung, L. H.; Liu, B. B.; Leung, F. K. C. Photocontrolled Chiral Supramolecular Assembly of Azobenzene Amphiphiles in Aqueous Media. *Polym. J.* **2023**, *55* (11), 1189–1198. https://doi.org/10.1038/s41428-023-00792-7.

(35) Cheung, L. H.; Kajitani, T.; Leung, F. K. C. Visible-Light Controlled Supramolecular Transformations of Donor-Acceptor Stenhouse Adducts Amphiphiles at Multiple Length-Scale. *J. Colloid Interface Sci.* **2022**, *628*, 984–993. https://doi.org/10.1016/J.JCIS.2022.08.034.

(36) Hung, K. L.; Cheung, L. H.; Ren, Y.; Chau, M. H.; Lam, Y. Y.; Kajitani, T.; Leung, F. K. C. Supramolecular Assemblies of Amphiphilic Donor–Acceptor Stenhouse Adducts as

Macroscopic Soft Scaffolds. *Beilstein J. Org. Chem.* **2024**, *20* (1), 1590–1603. https://doi.org/10.3762/BJOC.20.142.

(37) Yau, J. C. K.; Hung, K. L.; Ren, Y.; Kajitani, T.; Stuart, M. C. A.; Leung, F. K. C. Red-Light-Controlled Supramolecular Assemblies of Indigo Amphiphiles at Multiple Length Scales. *J. Colloid Interface Sci.* **2024**, *662*, 391–403. https://doi.org/10.1016/J.JCIS.2024.02.075.

(38) Shiraishi, Y.; Takagi, S.; Yomo, K.; Hirai, T. Spontaneous Isomerization of a Hydroxynaphthalene-Containing Spiropyran in Polar Solvents Enhanced by Hydrogen Bonding Interactions. *ACS Omega* **2021**, *6* (51), 35619–35628. https://doi.org/10.1021/ACSOMEGA.1C05400/ASSET/IMAGES/LARGE/AO1C05400_0007.JPEG.

(39) Shiraishi, Y.; Itoh, M.; Hirai, T. Thermal Isomerization of Spiropyran to Merocyanine in Aqueous Media and Its Application to Colorimetric Temperature Indication. *Phys. Chem. Chem. Phys.* **2010**, *12* (41), 13737–13745. https://doi.org/10.1039/C0CP00140F.

Table of Content